Astron. Astrophys. 344, 68–82 (1999)

ASTRONOMY AND ASTROPHYSICS

# A multiwavelength comparison of COMPTEL 1.8 MeV $^{26}$Al line data

**J. Knödlseder[1], K. Bennett[5], H. Bloemen[3], R. Diehl[2], W. Hermsen[3], U. Oberlack[6], J. Ryan[4], V. Schönfelder[2], and P. von Ballmoos[1]**

[1] Centre d'Etude Spatiale des Rayonnements, CNRS/UPS, B.P. 4346, F-31028 Toulouse Cedex 4, France
[2] Max-Planck-Institut für Extraterrestrische Physik, Postfach 1603, D-85740 Garching, Germany
[3] SRON-Utrecht, Sorbonnelaan 2, 3584 CA Utrecht, The Netherlands
[4] Space Science Center, University of New Hampshire, Durham, NH 03824, USA
[5] Astrophysics Division, ESTEC, ESA, 2200 AG Noordwijk, The Netherlands
[6] Astrophysics Laboratory, Columbia University, New York, NY 10027, USA

Received 7 July 1998 / Accepted 23 December 1998

**Abstract.** We search for correlations between 1.809 MeV $\gamma$-ray line emission, attributed to the radioactive decay of $^{26}$Al, and intensity distributions observed at other wavelengths by confronting *CGRO* COMPTEL 1.8 MeV data with an extended database of all-sky maps. The database contains 31 all-sky maps, covering the entire explored wavelength range from the radio band up to high-energy gamma-rays. Different data analysis techniques are explored to determine the similarities between the all-sky maps and the 1.809 MeV intensity distribution, and to estimate the systematic uncertainties of our study. The comparison shows that tracers of the old stellar population or the local interstellar medium provide only a poor description of COMPTEL 1.8 MeV data. Tracers of the young stellar population considerably improve the fit, confirming our earlier claims that $^{26}$Al nucleosynthesis is associated to massive stars. Residuals are minimal for the 53 GHz free-free emission map that has been obtained by *COBE* DMR at microwave wavelengths. Within the statistics of the present data, this tracer provides an entirely satisfactory fit to COMPTEL 1.8 MeV data. Thus, a correlation has been discovered, linking galactic $^{26}$Al nucleosynthesis to galactic free-free emission which is a tracer of the ionised interstellar medium.

**Key words:** nuclear reactions, nucleosynthesis, abundances – methods: data analysis – stars: early-type – Galaxy: stellar content – gamma rays: observations

## 1. Introduction

The 1.809 MeV gamma-ray line emission attributed to the radioactive decay of $^{26}$Al provides a valuable tracer of recent nucleosynthetic activity in our Galaxy. As a by-product of nucleosynthesis, $^{26}$Al has been proposed to be produced during core-collapse supernovae, during nova outbursts, by Asymptotic Giant Branch (AGB) stars, and by massive stars, in particular during the Wolf-Rayet (WR) phase. In addition to stellar production, $^{26}$Al can also be produced by spallation reactions of high-energy cosmic rays, although at substantially lower rates (for a recent review see Prantzos & Diehl 1996).

The COMPTEL telescope aboard the Compton Gamma-Ray Observatory (*CGRO*) provided the first imaging survey in the 1.809 MeV $\gamma$-ray line, and established a first map of the observed emission (Diehl et al. 1995). Extending these imaging studies, COMPTEL presents now an all-sky survey in the 1.809 MeV $\gamma$-ray line at a sensitivity level of $\sim 10^{-5}$ ph cm$^{-2}$ s$^{-1}$ (Oberlack et al. 1996). Different data analysis methods emphasise different aspects of the data, and it is important to recognise such biases for the scientific interpretation of the measurements. To exploit the COMPTEL measurements, we therefore follow complementary strategies which can be divided into two classes: (1) image reconstruction, providing an overall estimate of the 1.8 MeV intensity distribution without imposing astrophysical constraints on the admissible solutions, and (2) testing of specific astrophysical hypotheses (i.e. 1.809 MeV source distribution models) by means of model fitting.

Image reconstruction using the maximum entropy method (Strong et al. 1992) has revealed irregular and lumpy 1.809 MeV emission along the galactic plane with peculiar emission features towards Cygnus, Vela, Carina, and near the anticentre (Diehl et al. 1995; Oberlack et al. 1996). Such irregular emission is indeed expected if massive stars are at the origin of galactic $^{26}$Al, reflecting the spiral structure of our Galaxy (Prantzos 1991, 1993). It has gradually become clear, however, that the observed emission clumping reflects at least partially the statistical fluctuations of the data, leading to considerable difficulties for the interpretation of the sky maps (Knödlseder et al. 1996b). For this reason, alternative image reconstruction algorithms have been investigated which enlarge the range of acceptable maps of the 1.809 MeV sky (Fig. 1). This clearly demonstrates that astrophysical answers through image reconstruction are limited, and alternative analysis strategies have to be pursued.

Testing specific astrophysical hypotheses in COMPTEL's data space is such an alternative strategy. On the one hand, COMPTEL 1.8 MeV data have been compared to 3-dimensional

*Send offprint requests to*: Jürgen Knödlseder (knodlseder@cesr.fr)

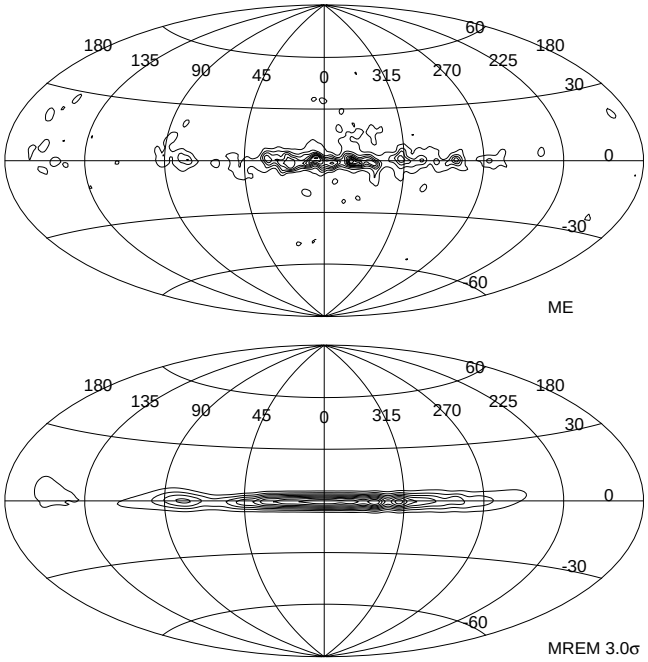


**Fig. 1.** COMPTEL 1.8 MeV all-sky maps as obtained by the maximum entropy (ME) method and the Multiresolution Regularized Expectation Maximization (MREM) algorithm. ME and MREM are complementary imaging methods. While ME emphasises point source emission with the drawback of representing smooth diffuse emission as irregular and lumpy structures, MREM reliably recovers significant emission structures with the drawback of suppressing hints for weak point source emission (for more details see Knödlseder et al. 1999).

geometrical models of the Galaxy in order to establish characteristic parameters of the $^{26}$Al source distribution (Diehl et al. 1995; Knödlseder et al. 1996a; Diehl et al. 1997). On the other hand, 1.8 MeV data have been correlated with plausible tracers of $^{26}$Al nucleosynthesis obtained from other fields of astronomy (Diehl et al. 1995; Diehl et al. 1997). Since from earlier results it was expected that massive stars are among the most plausible sources of $^{26}$Al in the Galaxy (Prantzos & Diehl 1996), recent research on $^{26}$Al modelling focused on finding optimum tracers of massive stars in the Galaxy (Diehl et al. 1996; Diehl et al. 1997). However, all attempts to fit COMPTEL 1.8 MeV data by plausible model distributions of proposed $^{26}$Al candidate sources have been inconclusive so far, since no-one of the tested $^{26}$Al tracers represents the observed intensity contrast between inner Galaxy to outer disk regime, nor accounts for the particularly bright emission regions in Cygnus, Vela, and Carina (Diehl et al. 1997).

In order to find a tracer which accurately describes the 1.8 MeV intensity distribution, we enlarge in this work our set of 'plausible model distributions' to an extensive database of all-sky maps, obtained throughout the entire observed wavelength range, starting at the $\lambda \sim 10$ m radio band up to the energetic $E > 100$ MeV $\gamma$-ray photons. In particular, we did not restrict ourselves to a physically motivated set of tracer maps which eventually could have prevented the discovery of an adequate 1.8 MeV tracer in the past. Since the Galaxy is transparent to $\gamma$-rays, each all-sky map of our database represents a specific hypothesis about the galactic distribution of $^{26}$Al. Hence the results of the tracer map comparison may be interpreted in terms of these hypotheses, providing physical insight into the origin of galactic $^{26}$Al. The comparison of the overall intensity distributions makes the analysis most sensitive to large-scale intensity contrasts and overall emission asymmetries in the data. Consequently, understanding these contrasts and asymmetries gives valuable information about the principal source of radioactive $^{26}$Al in the Galaxy.

This paper is organised as follows: In Sect. 2 we introduce the all-sky map database which was used for the comparison. Sect. 3 presents the analysis methods used as well as the results of the multiwavelength comparison. The results will be discussed in Sect. 4 and we conclude in Sect. 5.

## 2. Multiwavelength all-sky map database

### *2.1. General*

For the purpose of our comparison we built up a database of all-sky maps covering the entire explored wavelength range. We restricted ourselves to all-sky maps since we want to analyse the global distribution of 1.8 MeV emission with the aim of finding global tracers of galactic $^{26}$Al. The only exception in our sample is the CO map of Dame et al. (1987) which is restricted to galactic latitudes $|b| \leq 10^\circ - 30^\circ$. This obviously introduces some bias in the analysis which we estimate, however, to be rather small since most of the CO and 1.8 MeV emission is restricted to the galactic plane.

In the following we present the maps of our database. Some of them originally contained not only galactic emission but also instrumental or extragalactic diffuse background, or strong, mainly extragalactic point sources. When possible, these components have been removed from the maps, since we are looking for correlations between galactic emission processes. The final database is summarised along with the dominant emission mechanism and the intrinsic angular resolution of the maps in Table 1. For the purpose of the correlation study, the maps were convolved with the COMPTEL point spread function (PSF) which degrades their angular resolution to $3.8^\circ$ FWHM. Some of the maps have an intrinsic angular resolution which is worse than the COMPTEL resolution. The impact of angular resolution on the analysis results will be discussed below.

### *2.2. The all-sky maps*

The only all-sky survey available which traces galactic synchrotron radiation at the same frequency and with similar telescope beamsize is the Bonn 408 MHz survey of Haslam et al. (1982). For the analysis, the isotropic extragalactic background, which arises from cosmic background radiation and the sum of unresolved distant radio sources, was removed by subtracting 6 K from the observed antenna temperatures (Phillipps et al. 1981). Additionally, the brightest point-like sources in the map, mostly radio galaxies, were removed by

**Table 1.** The multiwavelength all-sky map database which was used for the 1.8 MeV correlation study. Maps marked by † are the models of Bennett et al. (1992) which have been used to extract free-free emission from DMR data. For maps marked by * several map modifications of the original data were compared to the 1.8 MeV sky (see text). Specified dust temperatures were calculated from the Wien law.

| Name | Emission mechanism | Tracer of ... | Resolution | Reference |
|---|---|---|---|---|
| 408 MHz | synchrotron | cosmic rays / magnetic field | $0.85^\circ$ | Haslam et al. (1982) |
| 21 cm | H hyperfine transition | neutral hydrogen | $1^\circ$ | Dickey & Lockman (1990) |
| DMR 31.5 GHz | free-free / synchrotron | ionised gas / cosmic rays | $7^\circ$ | Bennett et al. (1996) |
| DMR 53 GHz | free-free / synchrotron | ionised gas / cosmic rays | $7^\circ$ | Bennett et al. (1996) |
| 53 GHz synch.† | synchrotron | cosmic rays / magnetic field | $7^\circ$ | Bennett et al. (1992) |
| 53 GHz free-free | free-free | ionised gas | $7^\circ$ | Bennett et al. (1992) |
| 53 GHz dust † | thermal dust | dust | $7^\circ$ | Bennett et al. (1992) |
| DMR 90 GHz | free-free / synchrotron | ionised gas / cosmic rays | $7^\circ$ | Bennett et al. (1996) |
| CO* | CO rotational transition | molecular gas | $0.5^\circ$ | Dame et al. (1987) |
| DIRBE 240 $\mu$m * | thermal dust | dust ($T \sim 12$ K) | $0.7^\circ$ | Hauser et al. (1998) |
| FIRAS 205 $\mu$m | $N^+$ ($^3P_1 - ^3P_0$) | low-density ionised gas | $7^\circ$ | Wright et al. (1991) |
| FIRAS 158 $\mu$m | $C^+$ ($^2P_{3/2} - ^2P_{1/2}$) | neutral gas cooling | $7^\circ$ | Wright et al. (1991) |
| DIRBE 140 $\mu$m * | thermal dust | warm dust ($T \sim 21$ K) | $0.7^\circ$ | Hauser et al. (1998) |
| DIRBE 100 $\mu$m * | thermal dust | warm dust ($T \sim 30$ K) | $0.7^\circ$ | Hauser et al. (1998) |
| DIRBE 60 $\mu$m * | thermal dust | warm dust ($T \sim 50$ K) | $0.7^\circ$ | Hauser et al. (1998) |
| DIRBE 25 $\mu$m * | thermal dust / star light | warm dust ($T \sim 120$ K) / AGBs | $0.7^\circ$ | Hauser et al. (1998) |
| DIRBE 12 $\mu$m * | thermal dust / star light | warm dust ($T \sim 250$ K) / AGBs | $0.7^\circ$ | Hauser et al. (1998) |
| DIRBE 4.9 $\mu$m * | star light | stars (K and M giants) | $0.7^\circ$ | Hauser et al. (1998) |
| DIRBE 3.5 $\mu$m * | star light | stars (K and M giants) | $0.7^\circ$ | Hauser et al. (1998) |
| DIRBE 2.2 $\mu$m * | star light | stars (K and M giants) | $0.7^\circ$ | Hauser et al. (1998) |
| DIRBE 1.25 $\mu$m * | star light | stars (K and M giants) | $0.7^\circ$ | Hauser et al. (1998) |
| Visible | star light | stars | $< 1.0^\circ$ | Lund Observatory |
| TD1 274.0 nm | star light | nearby hot stars | $1^\circ$ | Thompson et al. (1978) |
| TD1 236.5 nm | star light | nearby hot stars | $1^\circ$ | Thompson et al. (1978) |
| TD1 196.5 nm | star light | nearby hot stars | $1^\circ$ | Thompson et al. (1978) |
| TD1 156.5 nm | star light | nearby hot stars | $1^\circ$ | Thompson et al. (1978) |
| ROSAT $1/4$ keV | thermal bremsstrahlung | local hot gas | $2.0^\circ$ | Snowden et al. (1993) |
| ROSAT $3/4$ keV | thermal bremsstrahlung | hot gas | $2.0^\circ$ | Snowden et al. (1993) |
| ROSAT $1.5$ keV | thermal bremsstrahlung | hot gas / X-ray binaries | $2.0^\circ$ | Snowden et al. (1993) |
| HEAO-1 | thermal bremsstrahlung | X-ray binaries | $3^\circ \times 1.5^\circ$ | Rothschild et al. (1979) |
| EGRET $> 100$ MeV | nuclear interactions | interstellar gas / cosmic rays | $2.0^\circ$ | HEASARC |

estimating the diffuse galactic intensity at the source position from the mean intensity in annuli around the sources.

Atomic neutral hydrogen (H I) is readily observed in emission by its 21 cm hyperfine line at 1420.4058 MHz. In this work, the H I map presented by Dickey & Lockman (1990) is used. The emission is given in units of hydrogen column density $N_{\rm H}$, and assumes optically thin emission.

At microwave frequencies, the galactic continuum emission becomes a mixture of synchrotron radiation of relativistic electrons, free-free emission from ionised matter, and thermal dust emission. For the comparison, the four year full-sky maps derived by the Differential Microwave Radiometers (DMR) instrument aboard the *Cosmic Background Explorer (COBE)* at $31.5$, $53$, and $90$ GHz were used (Bennett et al. 1996). The intensity distribution for the two DMR channels A and B have been averaged by weighting with the statistical uncertainties in individual sky map pixels. The zero level was determined from the mean intensity in the DMR maps above $|b| > 40^\circ$. Note that the DMR horn antennas have a full-width at half power of 7°, hence the angular resolution of the sky maps is inferior to that of COMPTEL data.

The different spatial and spectral morphology of the dominant emission processes may be used to separate these components in DMR microwave data. Using a model of galactic synchrotron emission based on the 408 MHz and the 1420 MHz radio surveys and a model of thermal dust emission based on *COBE* FIRAS data, Bennett et al. (1992) created the first all-sky map of free-free emission. This map, which traces the distribution of ionised matter throughout the entire Galaxy, will also be compared to the 1.8 MeV data. The synchrotron and dust models used by Bennett et al. (1992) for the component separation are included in the database for comparison.

The distribution of molecular hydrogen ($H_2$) is traced by a spectral line of CO at $\lambda = 2.6$ mm, arising from the first rotational level ($J = 1 \rightarrow 0$) excited by collisions with $H_2$ molecules. The CO emission intensity turns out to be proportional to the $H_2$ mass, hence it is a valuable tool for studies of the molecular mass distribution in the Galaxy (Combes 1991). This may not hold in the vicinity of the galactic centre, where the $H_2$ column density may be significantly lower than that inferred from CO observations (Sodroski et al. 1995).

The most complete survey of CO emission is the Columbia / Cerro-Tololo survey of Dame et al. (1987) which covers the entire Milky Way with latitude extent $|b| \leq 10^\circ - 30^\circ$. Due to the uncertainties in the $H_2$/CO conversion ratio in the galactic centre, two different maps were used for the comparison: the first consists of the original CO map of Dame et al. (1987) which shows a strong intensity peak towards the galactic centre. For the second map, this peak was removed by estimating the underlying diffuse emission from the longitude intervals $4.5^\circ < |l| < 5.5^\circ$ for latitudes below $|b| < 1.5^\circ$.

With its 10 photometric bands from 1 to 240 $\mu$m, the Diffuse Infrared Background Experiment (DIRBE) aboard the *COBE* satellite provides an almost complete coverage of the infrared (IR) wavelength range with adequate angular resolution of $0.7^\circ$ (Boggess et al. 1992). In the far-infrared (FIR) wavelength range from $\lambda \sim 40$–$1000$ $\mu$m, for which the Galaxy is optically thin, the galactic large-scale emission arises primarily from the cooling of radiatively heated large dust grains which attained an equilibrium temperature in the ambient radiation field. In the mid-infrared (MIR) wavelength range 5 $\mu$m $< \lambda <$ 40 $\mu$m, extensive dust emission is seen from the Galaxy which is believed to come from small grains ($\leq 0.01$ $\mu$m) briefly heated to high temperatures ($T \sim 100$ K) each time they absorb a single photon (Boulanger & Pérault 1988). Additionally, low-mass AGB stars are the most important point source component of the MIR sky. In the near-infrared (NIR) domain (1 $\mu$m $< \lambda <$ 5 $\mu$m), stellar emission, mainly from late K and M giants, becomes the dominant source of IR radiation. For the 1.8 MeV comparison, the 'DIRBE Zodi-Subtracted Mission Average Maps' (Hauser et al. 1998) were used, from which the zodiacal light contribution has been subtracted. Nevertheless, residual zodiacal light remains in the 12 $\mu$m and 25 $\mu$m maps. For reference, the original DIRBE maps including the zodiacal light component will also be compared to the data.

Embedded in the FIR continuum are spectral lines arising from transitions of atoms in the gaseous phase of the ISM. The most prominent of these gas cooling lines are the 158 $\mu$m ground state transition of $C^+$, the dominant heat loss mechanism for neutral gas in the Galaxy, and the 205 $\mu$m transition of $N^+$, tracing the large-scale low-density extended ionised component of the Galaxy (Bennett et al. 1994). Both lines have been successfully mapped by the Far-Infrared Absolute Spectrophotometer (FIRAS) aboard the *COBE* satellite with an effective angular resolution of 7° (Wright et al. 1991; Bennett et al. 1994). Note, however, that both maps are subject to substantial statistical uncertainties, and $\sim 5\%$ of the sky is not covered by the data. In particular, a bright emission feature in the Cygnus regions suffers from incomplete coverage.

The distribution of visible light (400 nm $< \lambda <$ 700 nm) fits continuously to the NIR intensity distribution. Owing to the strong extinction by interstellar dust, the light is primarily from stars within $\sim$ 1 kpc of the Sun. For the analysis, the 'Lund Observatory Milky Way Panorama' was used, transformed to the new galactic coordinate system. Note, however, that this panorama is based on a drawing under the supervision of Knut Lundmark, hence cannot be taken as a photometrically exact representation of the sky. Therefore, the results for this map, in particular the assigned flux value, should not be taken too literally. Nevertheless, unresolved stars in the densely populated galactic plane are accurately represented, and the overall effect is photographic in quality (Nilsson, private communication).

In the UV waveband, the sky is dominated by nearby hot stars of spectral type O and B aligned in a band on the sky known as Gould's belt. UV all-sky maps were constructed from the magnitude-limited catalogue of stellar ultraviolet fluxes obtained from the ESRO/TD1 satellite, which carried out a controlled scan of the whole sky (Thompson et al. 1978). For this purpose, the sky was pixelised in a cartesian coordinate grid of binsize $1^\circ \times 1^\circ$ and UV intensities of all point sources in the catalogue were accumulated in corresponding sky pixels. The choice of $1^\circ \times 1^\circ$ bins is arbitrary and of no importance for the purpose of our analysis since convolution with the COMPTEL PSF degrades the angular resolution to $3.8^\circ$ FWHM.

For the soft X-ray domain, the ROSAT all-sky maps of Snowden et al. (1993) were used, covering $\sim 98\%$ of the sky in the $\frac{1}{4}$ keV, $\frac{3}{4}$ keV, and 1.5 keV bands. Although discrete X-ray sources have not been removed from the maps, the angular resolution of $\sim 2^\circ$ emphasises low surface brightness extended features like nearby SNRs and the X-ray background.

At hard X-ray energies (3 keV $< E <$ 400 keV) the entire Galaxy becomes fully transparent to X-ray photons. The most prominent galactic sources seen in the hard X-ray sky are X-ray binaries and SNRs. In this work an all-sky map constructed from the combination of the HED3 and MED detectors of the *HEAO-1* A2 experiment was used (Rothschild et al. 1979). Conventionally, all-sky maps from this combination are analysed in a number of standard colours defined as weighted sums of counts from certain combinations of detector layers and pulse height channels (Allen et al. 1994). In this work, the R15 colour is used (1.5–60 keV). This is the most stable colour, since it is a sum of discovery scalers which did not change during the mission. Instrumental background was removed from the maps using the difference between the large and small FOV collimator configurations as described in Allen et al. (1994). To remove the isotropic cosmic background, a constant intensity was subtracted from the skymap which was estimated from regions at high galactic latitude devoid of prominent point sources. Additionally, some prominent extragalactic point-like sources have been removed from the map.

The outstanding feature of the high-energy gamma-ray sky (E $>$ 100 MeV) is diffuse radiation from the galactic plane, mainly arising from the interaction of cosmic-ray nuclei with the interstellar gas. For the analysis, the co-added four-years EGRET intensity all-sky map for energies E $>$ 100 MeV, provided by the NASA/Goddard Space Flight Center, was used. To account for cosmic diffuse background radiation, an isotropic intensity of $1.5\,10^{-5}$ ph cm$^{-2}$ s$^{-1}$ sr$^{-1}$ was subtracted from the map (Kniffen et al. 1996). In addition, to provide a map of the galactic diffuse emission, all sources from the Second EGRET Catalogue (Thompson et al. 1995) with a significance greater than $4\sigma$ have been removed.

## 3. All-sky map comparison

### *3.1. COMPTEL data representation*

COMPTEL allows the study of 1.8 MeV $\gamma$-ray line emission with an energy resolution of $\sim 8\%$ (FWHM) and an angular resolution of 3.8° (FWHM) within a wide field of view of about 1 steradian (Schönfelder et al. 1993). Data accumulation is divided into observation periods of constant viewing direction, lasting typically between 1–2 weeks. During an individual observation period a 1.8 MeV point source sensitivity of typically $6\,10^{-5}$ ph cm$^{-2}$ s$^{-1}$ is reached ($3\sigma$). Combination of observation periods allows on the one hand an important increase of sensitivity and on the other hand an extension of the field of view to the entire sky. In this work, data from $\sim 200$ viewing periods were combined to an all-sky dataset, covering $5$ years of continuous observations from May 1991 to June 1996 (observation periods 0.1–522.5). The resulting exposure has a maximum near the galactic centre with a point source sensitivity of $1.0\,10^{-5}$ ph cm$^{-2}$ s$^{-1}$ ($3\sigma$). The minimum of the exposure is located close to the southern galactic pole, the corresponding point source sensitivity is $1.5\,10^{-5}$ ph cm$^{-2}$ s$^{-1}$ ($3\sigma$).

COMPTEL measures incoming $\gamma$-ray photons by their consecutive interactions in two parallel detector planes where an incident photon is first Compton scattered in the upper layer and then absorbed (although often not completely) in the lower layer. From the energy deposits and the interaction locations in both layers, 4 fundamental event parameters are derived: the total energy deposit $E_{\rm tot}$, the Compton scatter angle $\bar{\varphi}$, and the scatter direction $(\chi, \psi)$. In principle, COMPTEL data should be analysed in this 4-dimensional data space, which, however, requires large amounts of computer resources that are not available to date. Consequently, the data are analysed in subspaces which are obtained by integration over some of the parameters. In this way, data analysis is sensitive to some aspect of the data, depending on the parameter over which the integration is performed.

Like all $\gamma$-ray telescopes, COMPTEL suffers from high instrumental background which is mainly due to activation of the telescope by high-energy cosmic-ray particles. Although the instrument incorporates passive and active background reduction (Schönfelder et al. 1993), more than $95\%$ of the registered events are still due to instrumental background. Hence, any accurate analysis of COMPTEL data requires a detailed knowledge of the distribution of the instrumental background events in the utilised data spaces.

### *3.2. Comparison in the imaging data space*

#### 3.2.1. Imaging data space

Model comparison, as well as image reconstruction, is usually performed in a 3-dimensional *imaging data space*, spanned by the Compton scatter angle $\bar{\varphi}$ and the scatter direction $(\chi, \psi)$ (Strong et al. 1992; Diehl et al. 1995). Analysis in this data space provides the highest angular resolution (3.8° FWHM), but most spectral information is lost. Nevertheless, this data space can be used for spectral analysis if the total energy deposit $E_{\rm tot}$ of the collected events is restricted to narrow intervals. As in previous works on the $1.809$ MeV line emission, we select the interval $E_{\rm tot} = 1.7$–$1.9$ MeV to optimise the sensitivity to $1.809$ MeV $\gamma$-rays.

The instrumental background is modelled following the approach of Knödlseder et al. (1996b) which is based on the event distribution in adjacent energy intervals. Time variabilities of the instrumental background between different observation periods were considered using the approach described by Oberlack (1997). The use of adjacent energy intervals for the generation of the background model incorporates additional spectral information in the analysis. Indeed, it has been shown that this model not only provides a satisfactory description of the instrumental background component but also suppresses possible continuum emission in the data analysis by more than $90\%$ (Knödlseder et al. 1996b). Hence, spatial analysis in the 3-dimensional imaging data space does indeed reveal 1.8 MeV line emission, although no detailed spectral information is used in this approach.

#### 3.2.2. Maximum likelihood analysis

Our standard method for model comparison consists in a maximum likelihood optimisation of the model parameters (de Boer et al. 1992). For this purpose, all maps of the database are convolved with the 3-dimensional COMPTEL point spread function to provide model distributions of expected 1.8 MeV source counts in the imaging data space. These source models are then fitted along with the instrumental background model to the data, where the scaling factor of the source model is a free parameter. The $\bar{\varphi}$ distribution of the instrumental background is not known a priori, hence we adjust this distribution by fitting all layers of the instrumental background model separately. Yet, we do not correctly determine the $\bar{\varphi}$ distribution of individual observation periods in this approach.

Besides the model parameters, the maximum likelihood analysis provides $-2\ln\lambda$ as a measure of the detection significance of the model on top of the background. $\lambda$ is the maximum likelihood ratio $L(B)/L(M+B)$, $B$ represents the background model, and $M$ the source model, i.e. the all-sky map convolved with the point spread function. Formally, $-2\ln\lambda$ obeys a $\chi^2_1$ probability distribution, hence the detection significance (in Gaussian $\sigma$) is given by $\sqrt{-2\ln\lambda}$.

To control the goodness-of-fit and to illustrate the correlation between the tracer maps and the 1.8 MeV emission, we determine longitude profiles of the residual counts along the galactic plane using a data projection technique called 'software-collimation' (Diehl et al. 1993). The use of longitude profiles is justified for this purpose since imaging analysis revealed that most of the 1.8 MeV emission is concentrated in the galactic plane (Oberlack et al. 1996). Software-collimation selects only those events from the 3-dimensional imaging data space that may have originated from a specific source at a given position $(l, b)$. Specifically, only those events are accepted for which $|\bar{\varphi} - \varphi_{\rm geo}| \leqq r$, where $r$ is the *acceptance*

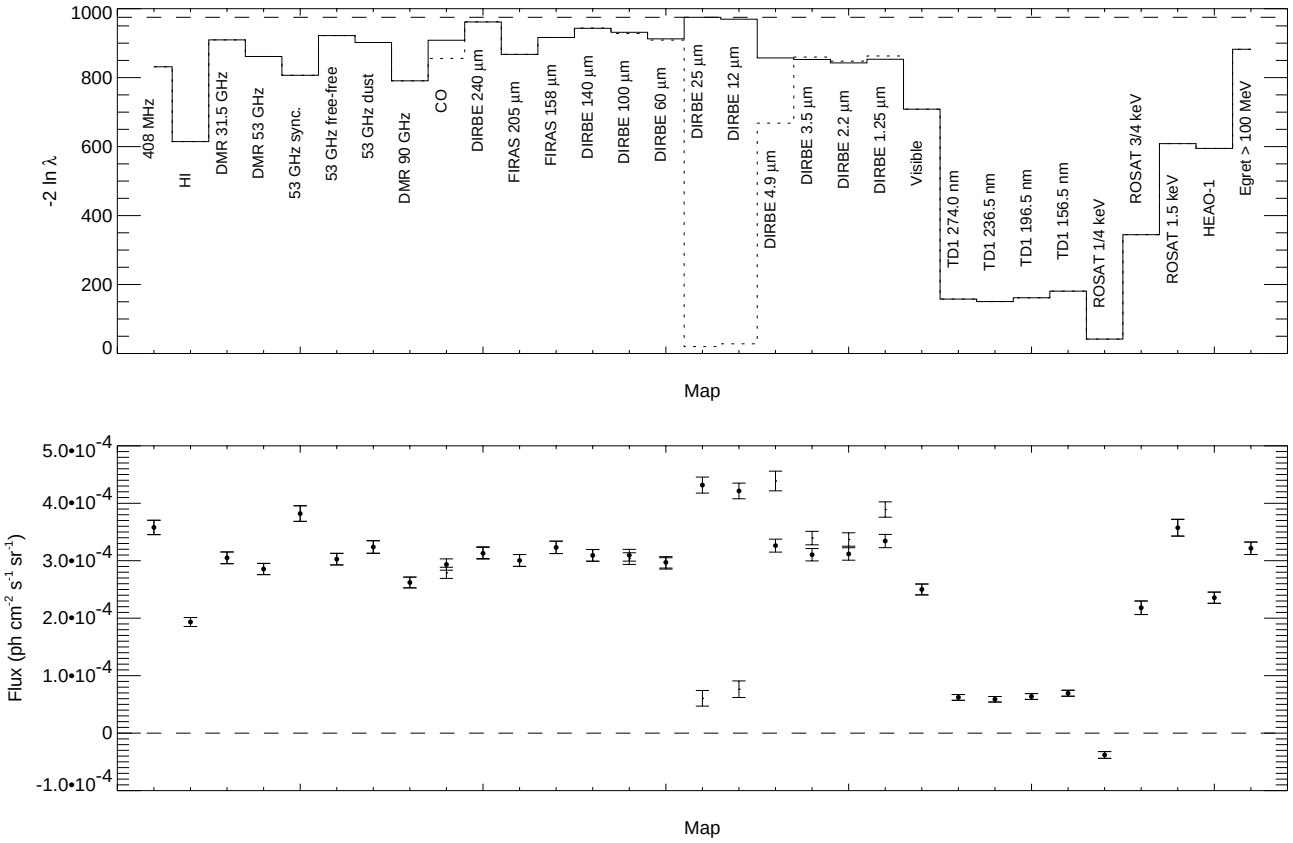


**Fig. 2.** Results of the multiwavelength maximum likelihood analysis. The top panel shows the quantity $-2\ln\lambda$ which measures the detection significance of the tracer map on top of the background. The solid histogram corresponds to the standard maps of the database, the dotted histogram is the result for some alternative maps (i.e., the CO map including the central peak and the DIRBE maps including the zodiacal light component; see text). Formally, the detection significance (in Gaussian $\sigma$) is given by $\sqrt{-2\ln\lambda}$. The best log-likelihood ratio of $-2\ln\lambda = 975$, which is obtained for the DIRBE 25 $\mu$m map, is indicated as dashed line. The bottom panel shows the flux that has been assigned to the central steradian of each all-sky map. Errorbars with dots correspond to the standard maps of the data base (solid histogram), undotted errorbars represents results for the alternative maps (dashed histogram).

*circle* which defines the angular extent of the source region, and $\varphi_{\rm geo} = \arccos(\sin\psi\sin b + \cos\psi\cos b\cos(\chi - l))$ is the expected scatter angle for events originating from the source position $(l, b)$. To determine longitude profiles, the number of events in the observed data space and the corresponding model components were determined by 'software-collimating' the data space for 120 equidistant positions along the galactic plane using an acceptance circle of $r = 3°$. This results in an effective angular resolution of $\sim 10°$ in the profiles. Note that adjacent points of the profile are not statistically independent since they partially share the same events.

The results of the maximum likelihood analysis are summarised in Fig. 2. Longitude profiles of the residual counts are shown for some representative all-sky maps in Figs. 3–4. The tracers which provide the smallest log-likelihood ratios are those which suffer from important galactic absorption. These are the all-sky maps from visible wavelengths up to soft X-rays (Visible - ROSAT $3/4$ keV). The domain of galactic absorption is clearly perceptible in Fig. 2 as a pronounced dip in the histogram of the log-likelihood ratios. Corresponding flux values are also systematically low. In particular, a negative flux is assigned to the ROSAT $1/4$ keV map. This map shows the Galaxy in absorption due to absorption of extragalactic X-ray background photons by galactic gas. Apparently, the data demand 1.8 MeV emission in the galactic plane, hence the best fit is obtained by inverting the X-ray map. This entirely confirms the imaging analysis of COMPTEL 1.8 MeV data which reveals the galactic plane as the most distinct emission feature (Oberlack et al. 1996). The residual longitude profiles of the TD1 274 nm and the ROSAT $1/4$ keV maps, shown in Fig. 3, support the maximum likelihood analysis. They clearly illustrate that COMPTEL 1.8 MeV data are not correlated to these tracer maps.

Maps in our database that are related to the old stellar population also provide only a poor description of the 1.8 MeV data. This is for example the case for the ROSAT 1.5 keV and HEAO-1 maps which trace the population of X-ray binaries. The longitude profile for the HEAO-1 map clearly demonstrates that the distribution of X-ray binaries is much more concentrated towards the inner Galaxy than the 1.8 MeV emission. The DIRBE near infrared maps at $\lambda \leq 4.9$ $\mu$m, tracing the population of K and M giants, can not explain the 1.8 MeV data either. Obviously, this population obeys a rather smooth and symmetric

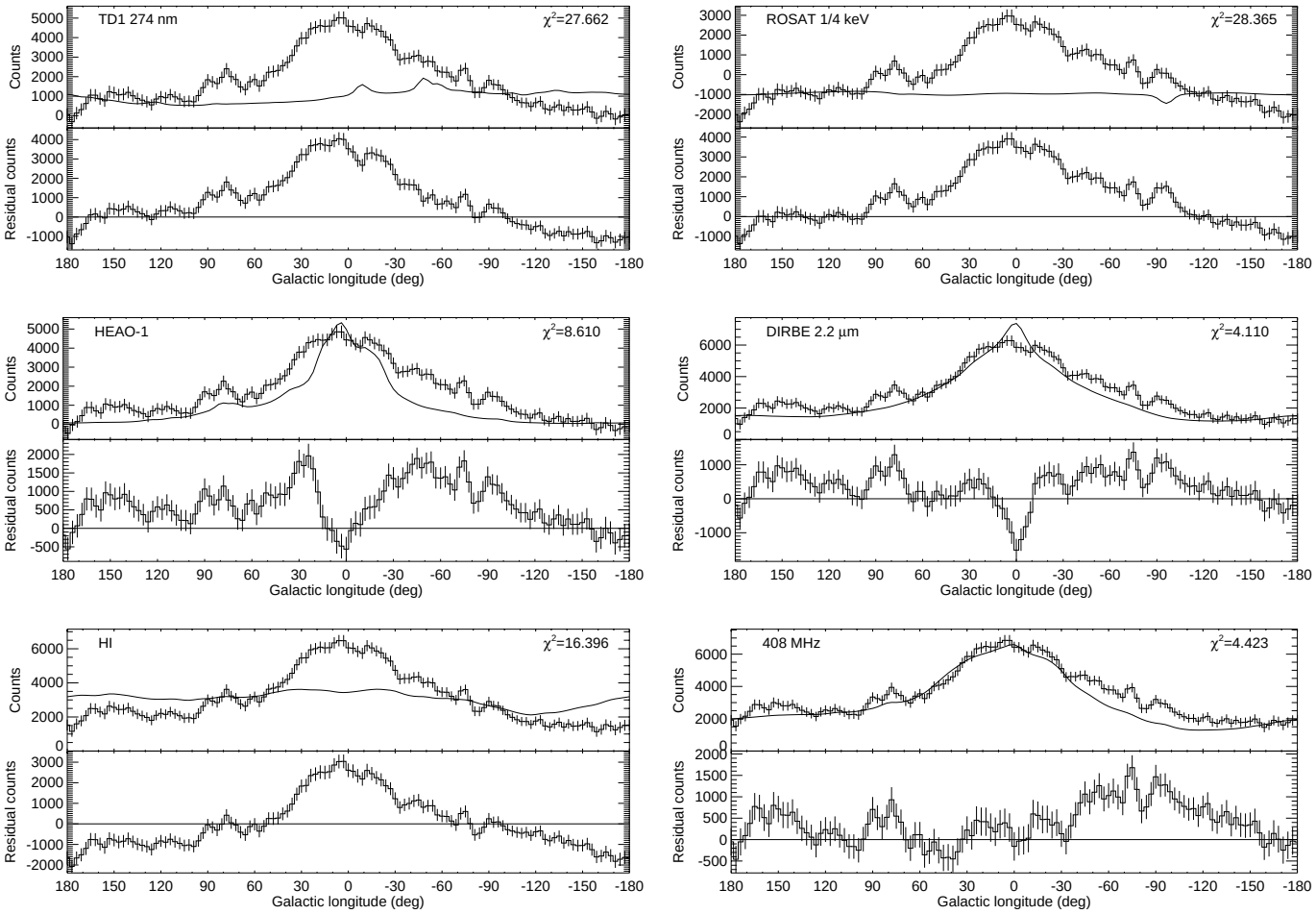


**Fig. 3.** Software collimator longitude scans for some of the all-sky maps. The histograms show the background subtracted 1.8 MeV counts, the solid lines show the corresponding all-sky map profiles convolved into the COMPTEL imaging data space. The reduced $\chi^2$ ($\chi^2/120$) values for the residual longitude profiles are quoted as measures of the correlation between the 1.8 MeV and the all-sky map longitude profiles. Note that adjacent points of the profile are not statistically independent, hence the reduced $\chi^2$ values should not be interpreted as the result of a statistical hypothesis test.

profile, in contrast to the structured and asymmetric distribution of the 1.8 MeV emission. Indeed, the population of K and M giants is usually modelled by a superposition of a probably bar-shaped bulge and an exponential disk with radial scale length between 1–3 kpc (Wainscoat et al. 1992), while fitting geometrical models to COMPTEL $1.8$ MeV data suggests a larger radial scale length of 5 kpc for the galactic distribution of $^{26}$Al (Diehl et al. 1997).

A very poor fit is also obtained for the atomic neutral hydrogen (H I) map. Obviously, the distribution of H I is much flatter than the 1.8 MeV emission profile (cf. Fig. 3). Considerably better, although not satisfactory fits are obtained for the synchrotron maps (408 MHz and 53 GHz sync.). They provide a reasonable fit for the inner Galaxy, but they clearly fail to describe the 1.8 MeV emission at negative longitudes and in the Cygnus region ($l \approx 80°$).

Another dip in the histogram of the log-likelihood ratios is seen for some DIRBE maps that still include the zodiacal light component (dotted histogram in Fig. 2). Zodiacal light arises from dust associated with the solar system, forming an extended emission band following the ecliptic. This band is inclined by $\sim 60°$ with respect to the galactic plane, leading to substantial high-latitude emission in some DIRBE maps. Particularly at mid-infrared energies (i.e. 12 $\mu$m and 25 $\mu$m) zodiacal light is the dominant emission component (Sodroski et al. 1997). The maximum likelihood analysis suggests that the 1.8 MeV data can not be described by such an emission component. However, if the zodiacal light component is removed from the DIRBE maps (solid histogram), the fits improve drastically, making the DIRBE 12 $\mu$m and 25 $\mu$m maps even to the tracer maps that provide the highest log-likelihood ratios.

The log-likelihood ratios for the best-fitting ($-2\ln\lambda > 875$) tracer maps are compiled in Fig. 5. The analysis suggests that the DIRBE 25 $\mu$m and 12 $\mu$m maps yield the best fit to COMPTEL 1.8 MeV data, followed by the DIRBE 240 $\mu$m, 140 $\mu$m, and 100 $\mu$m, and the 53 GHz free-free emission maps. However, the maximum likelihood analysis provides no framework to convert the differences between log-likelihood ratios for different

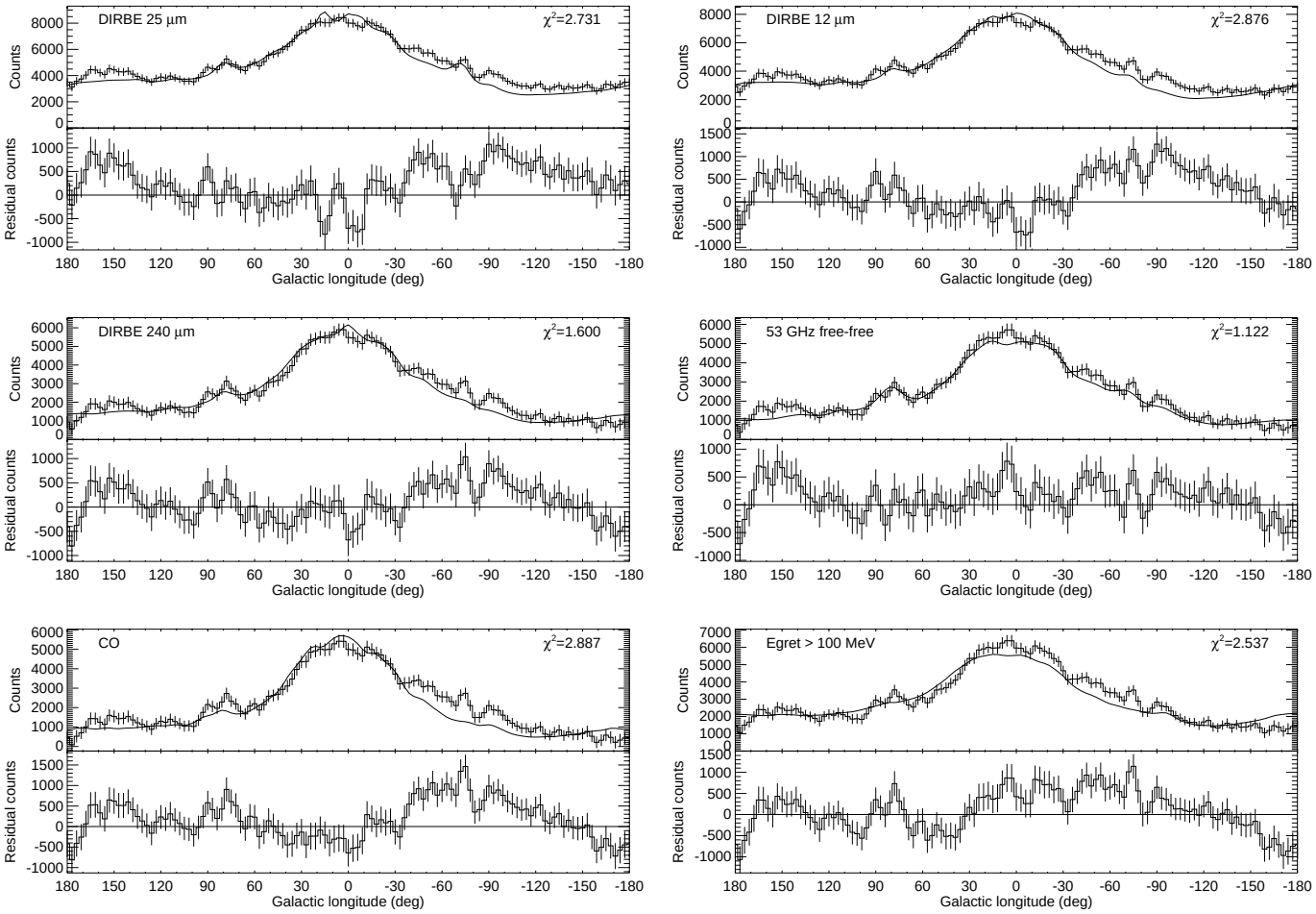


**Fig. 4.** Software collimator longitude scans for some of the best-fitting tracer maps.

tracer maps to statistical probability statements, hence we cannot judge from this analysis how significant the differences between the best tracer maps are. Nevertheless, comparison of the longitude profiles may illustrate the differences. Indeed, Fig. 4 demonstrates that all maps follow the 1.8 MeV intensity distribution rather closely. Yet, substantial residuals remain for some of the tracer maps. In particular, the DIRBE 25 $\mu$m and 12 $\mu$m maps which are suggested by the maximum likelihood analysis to present the best-fitting tracers show considerable residual emission towards negative longitudes, the galactic centre, and near the anticentre from $l = 130^\circ - 170^\circ$. In contrast, the 53 GHz free-free emission map, which takes only place 6 in the log-likelihood ratio ranking, provides much smaller residuals. Apparently, there is a certain bias in our analysis in that the tracer maps that maximise the likelihood ratio are not identical to those that minimise the 1.8 MeV residuals along the galactic plane.

Some bias in the likelihood analysis is expected from the different angular resolutions of the tracer maps. In particular, among the best-fitting tracers, the DMR and FIRAS maps have an angular resolution of only $7^\circ$ (FWHM) while the remaining maps have resolutions of the order of $1^\circ$ (FWHM). To study the impact of these differences on the analysis, we degraded the resolution of the best-fitting tracer maps to a common angular resolution of $7^\circ$ by convolving the maps with a Gaussian-shaped point spread function of adequate width (the DMR and FIRAS maps which already obey a resolution of $7^\circ$ have not been modified). The resulting log-likelihood ratios for the degraded maps are shown in Fig. 5 as dotted histogram. Degrading the angular resolution leads in all cases to a decrease of the log-likelihood ratios. This can be understood if the 1.809 MeV intensity distribution obeys a very narrow latitude profile that is considerably smaller than $7^\circ$ (FWHM). Indeed, fitting of double exponential disk models to COMPTEL 1.8 MeV data suggests a scale height for the $^{26}$Al distribution of 130 pc (Diehl et al. 1997), corresponding to a width of $\sim 3^\circ - 4^\circ$ (FWHM) for the 1.809 MeV latitude profile. This width is of the same order as the latitude profile of the DIRBE far-infrared or the CO maps. Consequently, smoothing the DIRBE and CO sky maps to a resolution of $7^\circ$ considerably widens their latitude profiles, and hence worsens their fit to the narrow 1.809 MeV intensity distribution.

Nevertheless, although the resolution degrading lowers the log-likelihood ratios, it is not sufficient to explain the discrepancy between the likelihood analysis and the residuals in the longitude profiles. In order to understand this discrepancy we have to re-consider the interpretation of the log-likelihood ra-

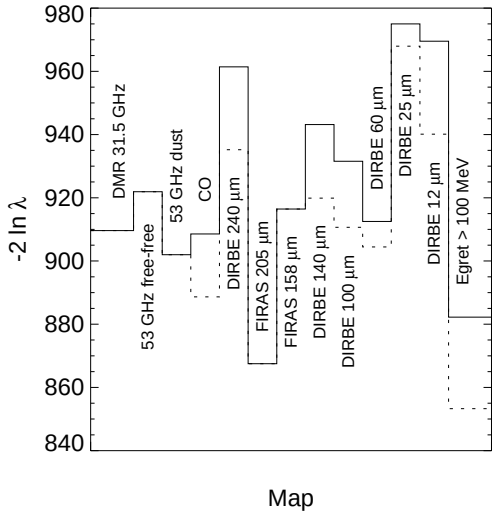


**Fig. 5.** Log-likelihood ratios for the 'best' ($-2\ln\lambda > 875$) tracer maps of the database. The solid histogram represent the results obtained for the standard maps. The dotted histogram shows the results after degrading the resolution of the maps to a common angular resolution of $7^\circ$ (see text).

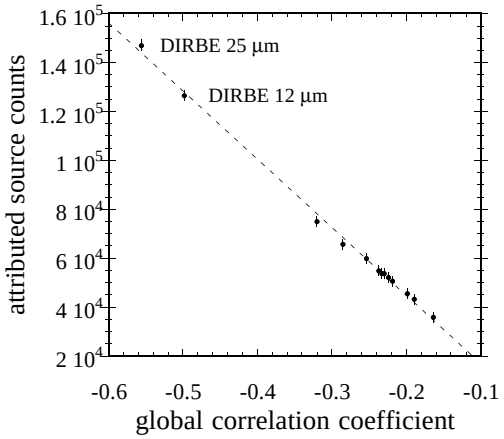


**Fig. 6.** Assigned number of source counts as function of the global correlation coefficient between the best-fitting tracer map data space models and the instrumental background model.

tios. In fact, the premise of the likelihood analysis is that the model we use to describe the instrumental background component is correct. Only in this case the log-likelihood ratio is a measure of the correlation between the 1.8 MeV $\gamma$-ray line intensity distribution and the tracer maps. In contrast, the background model we employ in this work is subject to systematic uncertainties, mainly due to the ignorance of the true $\bar{\varphi}$ distribution of the instrumental background (cf. 3.2.1). Hence, we formally only fit a combination of two data space models to the data and instrumental background counts may be partially attributed to the source component, or vice versa, if this improves the overall likelihood of the data. The possible confusion between the source and background component depends on the similarity of both models in the imaging data space. This similarity can be quantified by the *global correlation coefficient* (Eadie et al. 1982) which in our case will always be a negative quantity since rising one component will lower the other in order to conserve the total number of counts. It turned out that the global correlation coefficient depends mainly on the overlap of the source and background models in the imaging data space in the sense that more extended source models lead to higher correlations. As extreme examples we determined a global correlation coefficient of $-0.96$ for an isotrop sky model, while an isolated point source located at the galactic centre obeys only $-0.05$.

Indeed, we find a clear bias for our best-fitting tracer maps in the sense that more counts are attributed to the source component with increasing correlation between the source and background models (Fig. 6). This bias explains the relative high fluxes that have been attributed to the DIRBE 12 $\mu$m and 25 $\mu$m maps (cf. Fig. 2). In fact, although a model of zodiacal light emission has been removed from these maps, weak residual emission remains at high galactic latitudes, resulting in considerable correlation coefficients for these models. Accordingly, more source counts and hence higher fluxes are assigned. The bias does not explain, however, the high log-likelihood ratios that have been determined for these models. Although the correspondence of the peak in the histogram of log-likelihood ratios with the region of dominant zodiacal light emission is very suggestive for a possible bias, it is no proof and it could well be that there is an extended diffuse high-latitude 1.809 MeV component that is just better fitted by the DIRBE 12 $\mu$m and 25 $\mu$m tracer maps. In order to clarify this point, we will now investigate the 1.8 MeV residuals in more detail.

### 3.2.3. Residual analysis

For this purpose we determine 1.8 MeV $\gamma$-ray line residuals by means of a maximum likelihood ratio test (de Boer et al. 1992). Residual emission is searched by fitting point source models on top of the combined data space model (convolved tracer map + instrumental background model) for a grid of source positions. According to the above discussion the correlation coefficient between isolated point source models and the instrumental background component almost vanish, hence the results should not be biased by systematic uncertainties of the background model. Yet, the analysis can unveil regions where the background model reveals inappropriate.

The results of this residual point source search are complied in Fig. 7 for some of the best-fitting tracer maps. The quantity plotted is $-2\ln\lambda$, where $\lambda$ is the maximum likelihood ratio $L(M+B)/L(S+M+B)$, $M$ and $B$ represent the fitted all-sky map and background model, respectively, and $S$ the point source model which is moved over the entire sky on a grid of $64\,800$ source positions. In such a search, $-2\ln\lambda$ obeys a $\chi^2_3$ distribution. For comparison, the expected distributions for the ideal case of no residual 1.8 MeV emission and a correct instrumental background model are also shown (bottom-right panel). This 'ideal case' residual map was obtained by performing a

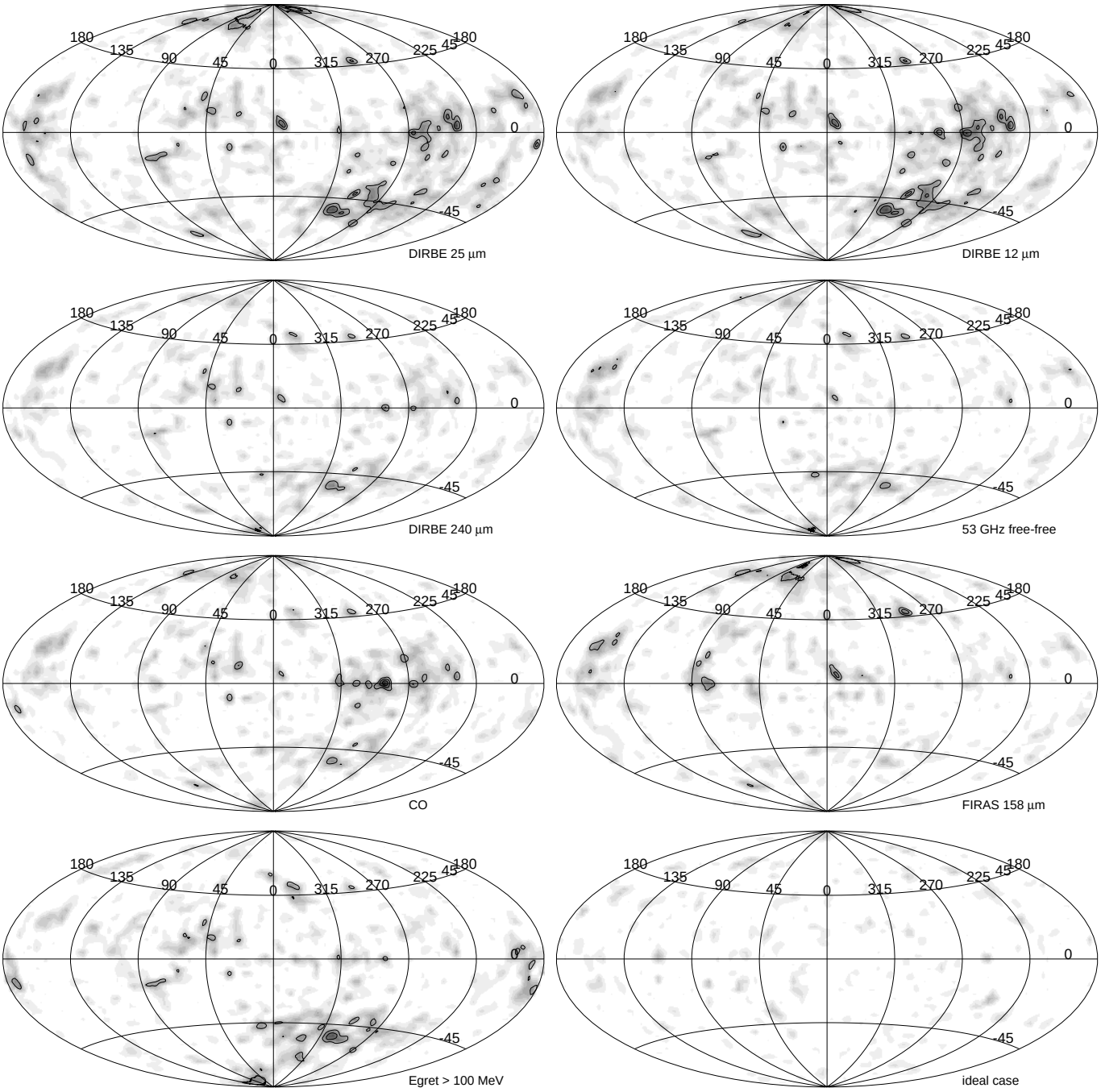


**Fig. 7.** Residual maximum likelihood ratio maps for some of the best-fitting all-sky maps. Contour levels correspond to detection significances of 3, 4, ... Gaussian $\sigma$ in a maximum likelihood point source search (3 d.o.f.). For reference, the residuals for an 'ideal case' (i.e. only statistical noise) are shown in the bottom-right panel.

residual analysis of a simulated model fit, where a mock dataset has been fitted by its parent data space model.

Obviously, the DIRBE 12 $\mu$m and 25 $\mu$m maps, which have provided the highest log-likelihood ratios in the maximum likelihood analysis, still show considerable 1.8 MeV residuals. On the one hand these are found in the galactic plane as already revealed by the software collimator longitude scans (cf. Fig. 4). On the other hand they appear at high galactic latitudes, mainly in regions where no residual zodiacal light emission is present in these tracer maps. Clearly, although their log-likelihood ratios have been worse, the other tracer maps show less residuals, hence they describe the 1.809 MeV intensity distribution more accurately.

In particular, residual 1.809 MeV emission is minimal when the 53 GHz free-free emission map is fitted to COMPTEL 1.8 MeV data. Only for this map no significant 1.8 MeV residual feature remains in the galactic plane. The DIRBE 240 $\mu$m map, which provides almost as few residuals as the 53 GHz free-free

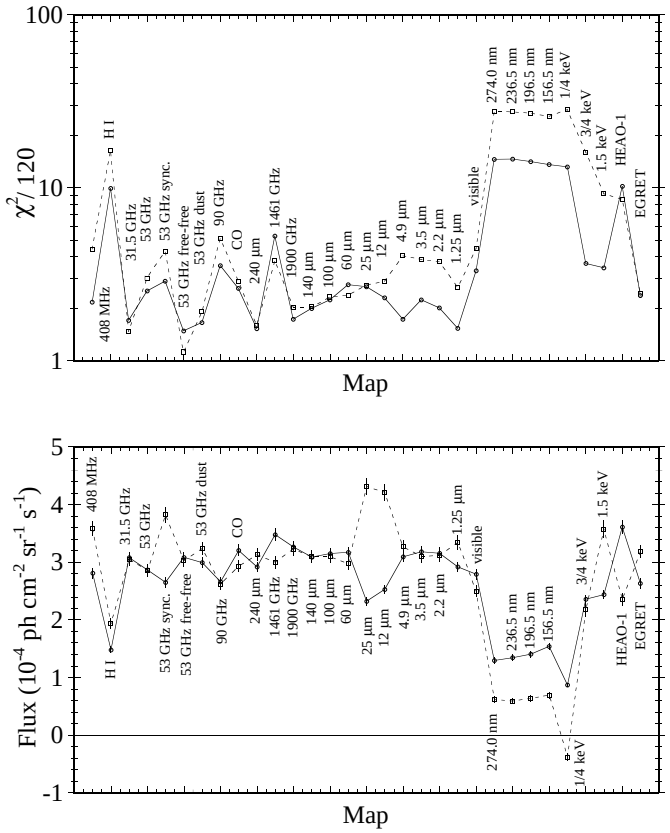


**Fig. 8.** Results of the multi-wavelength all-sky map comparison. Dots and solid lines correspond to analysis results in the energy data space, rectangles and dashed lines correspond to analysis results in the imaging data space. The top plot shows the reduced $\chi^2$ of the longitude profile, the bottom plot gives the corresponding flux values.

emission map, still shows significant residual 1.8 MeV emission towards Carina ($l \approx 286°$) and Vela ($\approx 266°$). Few residuals are also found for the FIRAS 158 $\mu$m map. The main discrepancy appears in the Cygnus region ($l \approx 80°$) where the FIRAS maps of our database obey incomplete sky coverage. Indeed, a brightened limb around the uncovered region indicates the possible presence of an emission peak in the 158 $\mu$m sky at this location. If we exclude this region for the maximum likelihood fitting and the residual analysis, the FIRAS 158 $\mu$m and the 53 GHz free-free emission maps describe the 1.8 MeV data equally well.

### *3.3. Comparison in the energy data space*

#### 3.3.1. Energy data space

As alternative to the imaging data space, $\gamma$-ray lines may be analysed in the energy data space which is spanned by the total energy deposit $E_{\rm tot}$. Spatial information, provided by the Compton scatter angle $\bar{\varphi}$ and the scatter direction $(\chi, \psi)$, is now used for primary event selection, a technique which was used before to generate longitude residual profiles. This software-collimation technique provides only poor angular resolution ($\sim 10°$ FWHM), but maximises the spectral information used in the analysis. Thus it is complementary to imaging data space analysis, and can be used to validate the results obtained above.

For the purpose of the all-sky map comparison, 120 source spectra were obtained for equidistant positions along the galactic plane ($b = 0°$) using an acceptance circle of $r = 3°$. The spectra were fitted by an analytical model for the instrumental background component plus a Gaussian of instrumental width ($\sigma = 59$ keV) at 1.809 MeV to measure the line signal. The analytical background model is composed of an exponential law to model the overall shape of the background and three Gaussians to describe particular background features in the spectra. These Gaussians model the 1.461 MeV line arising from radioactive decay of $^{40}$K within the instrument (fixed position and instrumental line width), the 2.223 MeV line arising from neutron capture in the upper detector layer (free position and width), and a feature around $\sim 1.48$ MeV which is attributed to cascade events originating from $^{22}$Na (free position and width). In all cases, this description led to satisfactory fits of the energy spectra from 1.3–2.4 MeV.

The fitted number of 1.809 MeV source counts define a longitude profile of the line emission along the galactic plane. Predicted number of source counts for the all-sky maps were determined by convolution of all maps with the instrumental point spread function and software-collimation of the resulting data spaces. These model longitude profiles were then fitted to the observed longitude scan. Flux errors for the spectral analysis were derived using Bootstrap sampling. Simple error propagation from spectral fitting results are not suitable since neighbouring scan positions are not statistically independent.

#### 3.3.2. Results

The resulting reduced $\chi^2$ values for the longitude profiles are shown in Fig. 8. Comparison with the results obtained from the software collimator scan in the imaging data space analysis shows that the two methods provide similar trends. This is remarkable since the imaging data space analysis made use of the entire COMPTEL all-sky data space for the analysis, i.e., a data space which covers the entire sky; in contrast, the spectral analysis made only use of galactic plane data, hence it is not very sensitive to high latitude emission. This also explains the main discrepancies: most maps which lead to significantly different results are maps which contain non-negligible high-latitude emission (e.g., 408 MHz, H I, 53 GHz sync., near IR maps, UV maps, X-ray maps). Obviously, restriction of the analysis to the galactic plane (i.e., omission of the high-latitude emission) improves the agreement between the all-sky maps and the 1.8 MeV data, supporting the finding that 1.809 MeV emission is concentrated on the galactic plane.

Flux determination with the two analysis methods also gives similar results, at least for the maps that show no significant high-latitude emission. In particular, for the 53 GHz free-free emission map spatial analysis results in $(3.03 \pm 0.10)\,10^{-4}$ ph cm$^{-2}$ s$^{-1}$ sr$^{-1}$ while spectral analysis gives $(3.09 \pm 0.09)\,10^{-4}$ ph cm$^{-2}$ s$^{-1}$ sr$^{-1}$ for the central steradian. This converts to intensities of $(2.8 \pm 0.1)\,10^{-4}$ ph cm$^{-2}$ s$^{-1}$ rad$^{-1}$

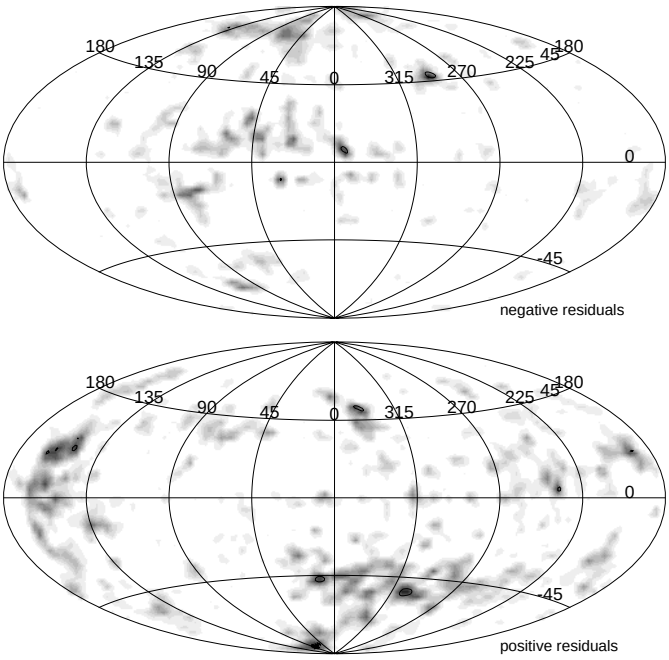


**Fig. 9.** Residual maximum likelihood ratio maps for the 53 GHz free-free emission map, separated into negative (top) and positive (bottom) flux residuals. Contour levels correspond to detection significanes of 3, 4, ... Gaussian $\sigma$ in a maximum likelihood point source search (3 d.o.f.).

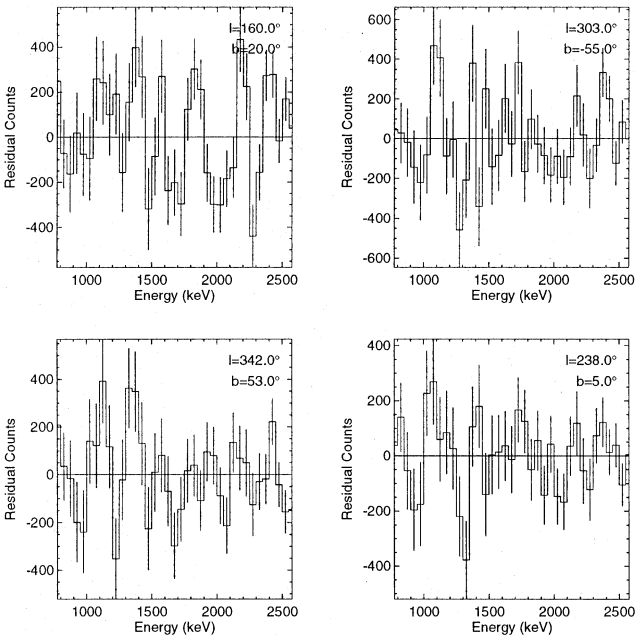


**Fig. 10.** Some background subtracted COMPTEL energy spectra towards locations of residual features in Fig. 9.

and $(2.9 \pm 0.1)\, 10^{-4}$ ph cm$^{-2}$ s$^{-1}$ rad$^{-1}$ for the central galactic radian if the map is integrated over $|b| < 20°$. Hence both methods, which use completely different background modelling and source detection techniques, provide consistent results. Note, however, that Bloemen et al. (1998), using an alternative background modelling method based on a data filtering technique, obtained a higher intensity of $\sim 4\, 10^{-4}$ ph cm$^{-2}$ s$^{-1}$ rad$^{-1}$ from the central radian. The discrepancy is probably explained by the different treatment of the instrumental background component, and reflects our current uncertainty for the determination of absolute 1.809 MeV flux values.

## 4. Discussion

### *4.1. The best 1.809 MeV tracer*

Imaging and energy data space analyses lead to the conclusion that the 53 GHz free-free emission map provides the best correlation to COMPTEL 1.8 MeV $\gamma$-ray line data. The software collimator scans presented in Fig. 4 illustrate that this is the only map which obeys the same pronounced intensity contrast in the Cygnus regions as found in the 1.8 MeV data. It is also the only map which provides a satisfactory description of the 1.8 MeV emission profile towards negative longitudes. It has been demonstrated that this map minimises the 1.8 MeV emission residuals, both in the longitude profile and in the point source search.

Nevertheless, some significant 1.8 MeV residuals remain in the data on top of the 53 GHz free-free emission map. This is illustrated in Fig. 9 where maximum likelihood ratio maps of residual 1.8 MeV emission are shown for this tracer map, splitted in features corresponding to negative (top) and features corresponding to positive (bottom) point source fluxes. There are extended positive residuals below galactic latitude $b < -30°$, extending over longitudes $240° - 30°$. Additional positive features are seen near the anticentre above the galactic plane between galactic longitudes $140° - 170°$ or localised around $(l, b) \approx (342°, 53°)$. We obtained software-collimated energy spectra for all of these features but no 1.8 MeV line signature could have been identified. Some examples are shown in Fig. 10 for locations where significant positive point source residuals are found in the analysis. The absence of 1.8 MeV line signatures towards the residuals suggests that these features are most probably due to uncertainties in the instrumental background model. This is supported by the fact that not only positive residuals are found. In the northern galactic pole area, negative residuals of comparable amplitude are seen in the map, indicating that the background model systematically overestimates the instrumental background in this region. Hence, positive residuals may correspondingly represent regions of systematic underestimation of the background component. It is worthwhile emphasising, however, that the amplitudes of the residuals are quite small compared to the 1.8 MeV signal from the Galaxy. Globally, the instrumental background model we use is quite accurate, but when local details or features close to the sensitivity limit are interpreted, the behaviour of the instrumental background model must be accounted for.

Thus, to the actual limit of the data analysis and sensitivity, the 53 GHz free-free emission map provides a satisfactory description of the entire 1.8 MeV intensity distribution. This means that we have assessed a simple tracer of 1.809 MeV

**Table 2.** Flux asymmetry as determined from some tracer maps. The intensity contrast of the tracer maps is given in column 2, asymmetry indices obtained by fitting splitted tracer maps to COMPTEL 1.8 MeV data are given in column 3 and 4 for imaging and energy data space analysis, respectively.

| Name | map | $\alpha_{\mp}$ imaging | energy |
|---|---|---|---|
| 53 GHz free-free | 1.03 | $1.02 \pm 0.07$ | $1.06 \pm 0.06$ |
| DIRBE 240 $\mu$m | 0.90 | $1.00 \pm 0.07$ | $0.98 \pm 0.06$ |
| CO | 0.81 | $0.97 \pm 0.07$ | $0.90 \pm 0.05$ |
| EGRET $> 100$ MeV | 0.92 | $1.04 \pm 0.06$ | $1.10 \pm 0.05$ |

emission which can help to understand the origin and distribution of galactic $^{26}$Al. It is simple in the sense that there is only one free parameter, namely the relative scaling of 53 GHz free-free emission to 1.809 MeV $\gamma$-ray line emission. Consistently, both analysis methods presented in this work give essentially the same scaling factor: imaging data space analysis suggests $0.86 \pm 0.03$ ph cm$^{-2}$ s$^{-1}$ sr$^{-1}$ K$^{-1}$ while spectral analysis results in $0.88 \pm 0.03$ ph cm$^{-2}$ s$^{-1}$ sr$^{-1}$ K$^{-1}$. The corresponding number of 1.809 MeV photons detected by COMPTEL amounts to $54\,000 \pm 1\,800$. The significance of the detection of the 53 GHz free-free emission map over background is $30\sigma$. Using a data filtering technique and estimates of the 1.8 MeV continuum emission based on model fits at adjacent energies to model the instrumental background component, Bloemen et al. (1998) derived a somewhat higher value of $1.35 \pm 0.06$ ph cm$^{-2}$ s$^{-1}$ sr$^{-1}$ K$^{-1}$ for the scaling factor between 53 GHz free-free and 1.809 MeV $\gamma$-ray line emission. This could point at a potential inclusion of a small signal component in our background as derived from adjacent energies.

### *4.2. Flux asymmetry*

Earlier analysis of COMPTEL 1.8 MeV data from the first year of the *CGRO* mission suggested a global asymmetry of 1.809 MeV emission with about $25\%$ - $65\%$ more 1.8 MeV flux from negative longitudes ($-180^\circ < l < 0^\circ$) than from positive longitudes ($0^\circ < l < 180^\circ$) (Diehl et al. 1995). On the contrary, the intensity contrast between negative and positive longitudes of the best-fitting tracer maps in our database is close to unity. This is illustrated in Table 2 where the asymmetry index $\alpha_{\mp}$, defined as the 1.809 MeV intensity ratio between $-180^\circ < l < 0^\circ$ and $0^\circ < l < 180^\circ$, integrated over $|b| \leq 30^\circ$, is shown for some of the tracer maps.

To address the question of a global flux asymmetry between negative and positive longitudes, we splitted the tracer maps at $l = 0^\circ$ into two halves and fitted both components simultaneously with independent scaling factors to the 1.8 MeV data. The resulting flux asymmetry indices are given in columns 3 and 4 of Table 2 for the imaging and energy data space analysis, respectively. Again, results obtained by both analysis methods are consistent within the statistical uncertainties.

The analysis suggests that there is no global flux asymmetry in the integrated 1.809 MeV emission from positive and from negative longitudes. For tracer maps with an intrinsic flux asymmetry, the fit scales both model components in a way that the flux asymmetry is reduced. Thus, although the longitude profiles of the 1.809 MeV emission and of the best-fitting tracer maps are rather asymmetric, the integrated 1.8 MeV intensities from both hemispheres are comparable. Apparently, the extended 1.809 MeV emission tail at negative longitudes ($-120^\circ < l < -30^\circ$), which is missing at positive longitudes, is compensated by an extended low-level emission at positive longitudes, reaching towards the anticentre (cf. Fig. 3). In our earlier analysis (Diehl et al. 1995), this low-level intensity was apparently missed due to the low exposure in this region, faking a global 1.809 MeV flux asymmetry for the Galaxy. The analysis presented in this paper shows that globally the 1.809 MeV intensities at positive and negative galactic longitudes are similar.

This is one of the reasons that many maps of the all-sky database are unable to provide a satisfactory fit to COMPTEL 1.8 MeV data. Most of the Population I tracers (CO, far-infrared, high-energy $\gamma$-rays) have asymmetry indices below unity ($\alpha_{\mp} \sim 0.8$–$0.9$), leaving important 1.8 MeV residuals at negative longitudes in the range $-150^\circ \lesssim l \lesssim -30^\circ$. The asymmetry of these tracers can be understood as an asymmetry in the distribution of local interstellar matter. For the CO map ($\alpha_{\mp} = 0.81$), most of the emission besides the inner-Galaxy ridge arises from local molecular clouds where the total cloud mass is 4 times greater at positive than at negative longitudes (Dame et al. 1987). Since FIR and the high-energy $\gamma$-ray maps are partly correlated to the molecular cloud distribution, they obey a similar trend. Obviously, COMPTEL 1.8 MeV data do not obey an equivalent flux asymmetry. The linearity between our tracers and 1.8 MeV emission only holds on larger spatial and time averages (e.g. Diehl et al. 1996); these may not be given in particular for preferntially local regions. Consequently, the flux asymmetry may be interpreted as either a low nucleosynthesis activity over the last million years in the local interstellar medium ($\lesssim 1$ kpc), or as enhanced activity towards negative longitudes, corresponding possibly to the Carina spiral arm. A further discussion of flux asymmetries in COMPTEL 1.8 MeV data based on image reconstructions is given by Oberlack (1997).

### *4.3. Inner to outer Galaxy contrast*

The software collimated longitude profiles obtained for imaging data space analysis (cf. Fig. 4) and energy data space analysis indicate that the 53 GHz free-free emission profile may slightly underestimate the 1.809 MeV intensity in the inner Galaxy ($|l| < 30^\circ$). To investigate if the inner to outer Galaxy contrast of 1.809 MeV $\gamma$-ray line and 53 GHz free-free emission are similar, we splitted the 53 GHz free-free emission map into two parts, one covering the inner Galaxy from $-30^\circ < l < 30^\circ$, and one covering the remaining outer Galaxy. Both components are then fitted simultaneously with independent scaling factors to the data. We define $\alpha_{i/o}$ as the ratio between inner to outer Galaxy

scaling factors. The fit in the imaging data space provides $\alpha_{i/o} = 0.93 \pm 0.10$ while analysis in the energy data space results in $\alpha_{i/o} = 1.09 \pm 0.10$.

Both results are still consistent with unity, although they show an opposite trend. Apparently, it is difficult to judge from this analysis whether there is indeed an enhanced inner to outer Galaxy contrast in COMPTEL 1.8 MeV data with respect to the 53 GHz free-free emission map. The difference in the trend illustrates the systematic uncertainties of both analysis methods. It is to be determined if further refinement of the analysis methods can reduce these uncertainties and actually improve the contrast determination. Considering the systematical and statistical uncertainties, we estimate that using current analysis techniques, a contrast around $30\%$ should be at the detection limit of COMPTEL.

## 5. Conclusions

The multiwavelength correlation study of COMPTEL 1.8 MeV data provides a unique tool for the understanding of 1.809 MeV $\gamma$-ray line emission. Firstly, it confirms that $^{26}$Al is a galaxy-wide phenomenon, a result that we already derived from image reconstructions of COMPTEL 1.8 MeV data (Diehl et al. 1995; Oberlack et al. 1996). Only those tracer maps that do not suffer from galactic absorption and hence represent galactic emission processes globally are capable of fitting the data, although most of them leave considerable residual emission when fitted to the data.

Secondly, tracers of the old stellar population can not describe the 1.8 MeV data properly. They leave significant residual excess 1.8 MeV emission in the outer Galaxy when fitted to the data. Apparently, Population I objects are much more concentrated towards the inner Galaxy than the galactic distribution of $^{26}$Al. Additionally, Population I objects do not reflect the galactic spiral structure; in contrast we find clear hints for spiral structure in our data (Knödlseder et al. 1996a), leading to considerable 1.809 MeV intensity asymmetries. Nevertheless, when averaged over the galactic plane, similar 1.8 MeV fluxes are found for positive ($l > 0°$) and negative ($l < 0°$) galactic longitudes.

Thirdly, tracers of the young stellar population fit considerably better to COMPTEL 1.8 MeV data than the Population I tracer maps. Yet, most of them can not describe all features of the data satisfactory, like the relative large 1.8 MeV emission at negative longitudes or the 1.8 MeV emission peaks towards Cygnus or Carina. Only the 53 GHz free-free emission map follows the data closely, leaving no significant 1.8 MeV emission along the galactic plane. Remaining weak residuals have to be studies carefully, as they may relate to systematic uncertainties in our instrumental background model. For example, significant residuals near the anticentre or the southern galactic pole area have been found to show no 1.809 MeV $\gamma$-ray line signature in the spectral analysis.

The discovery of the close correlation between 1.809 MeV emission and galactic free-free radiation provides an important clue for the understanding of galactic $^{26}$Al nucleosynthesis. Knödlseder (1999) showed that the correlation can be understood if the galactic $^{26}$Al mass density is directly proportional to the mass density of the ionised interstellar medium (ISM). Since the ionisation of the ISM is mainly provided by (very) massive stars (e.g., Abbott 1982; Reynolds 1984), he argues that these objects should also be the main source of galactic $^{26}$Al. Yet, he also illustrates that the galactic metallicity gradient could distort the correlation between 1.809 MeV and free-free emission, providing important insights in nucleosynthesis processes. With the current sensitivity of COMPTEL and the actual analysis techniques, we can not find such distortions. However, future gamma-ray telescopes with improved sensitivity and enhanced spectral as well as angular resolution will provide important new insights. In particular, the gamma-ray spectrometer SPI aboard of *INTEGRAL*, scheduled for launch in 2001, will help to determine the 1.809 MeV intensity distribution much more accurately, and hence provide an ideal tool for further dedicated correlation studies with its unique spectral resolution and improved sensitivity.

*Acknowledgements.* It is a pleasure to thank A. Kohnle, M. Leising, and G. Skinner for helpful discussions and comments. The author is supported by the European Community through grant number ERBFMBICT 950387. The COMPTEL project is supported by the German government through DARA grant 50 QV 90968, by NASA under contract NAS5-26645, and by the Netherlands Organisation for Scientific Research NWO. The COBE datasets were developed by the NASA Goddard Space Flight Center under the guidance of the COBE Science Working Group and were provided by the NSSDC. This research has made use of data obtained through the High Energy Astrophysics Science Archive Research Center Online Service, provided by the NASA/Goddard Space Flight Center. The research project has also benefit from financial support provided by the Cité de l'Espace in Toulouse.

## References

Abbott D.C.,1982, ApJ 263, 723
Allen J.S., Jahoda K., Whitlock L.A., 1994, Legacy 5, 27
Bennett C.L., Smoot G.F., Hinshaw G., et al., 1992, ApJ 396, L7
Bennett C.L., Fixsen D.J., Hinshaw G., et al., 1994, ApJ 434, 587
Bennett C.L., Banday K.M., Gorski G., et al., 1996, ApJ 464, L1
Bloemen H., Diehl R., Hermsen W., Knödlseder J., Schönfelder V., 1998, In: Proc. 3rd INTEGRAL Workshop, Taormina. Gordon & Breach, in press
Boggess N.W., Mather J.C., Weiss R., et al., 1992, ApJ 397, 420
Boulanger F., Pérault M., 1988, ApJ 330, 964
Combes F., 1991, ARA&A 29, 195
Dame T.M., Ungerechts H., Cohen R.S., et al., 1987, ApJ 322, 706
de Boer H., Bennett K., Den Herder J.W., et al., 1992, In: Di Gesù J., et al. (eds.) Data Analysis in Astronomy - IV, Plenum Press, New York, 241
Dickey J.M., Lockman F.J., 1990, ARA&A 28, 215
Diehl R., Bennett K., Bloemen H., et al., 1993, A&AS 97, 181
Diehl R., Dupraz C., Bennett K., et al., 1995, A&A 298, 445
Diehl R., Bennett K., Dupraz C., et al., 1996, A&AS 120, 321C
Diehl R., Oberlack U., Knödlseder J., et al., 1997, In: Dermer C.D., Strickman M.S., Kurfess J.D. (eds.) Proc. of the Forth Compton Symposium. AIP, New York, 1114

Eadie W.T., Drijard D., James F.E., Roos M., Sadoulet B., 1982, Statistical Methodes in Experimental Physics. North-Holland Publishing Company, 23
Haslam C.G.T., Stoffel H., Salter C.J., Wilson W.E., 1982, A&AS 47, 1
Hauser M.G., Kelsall T., Leisawitz D., Weiland J., 1998, COBE Ref Pub. No. 98-A (Greenbelt, MD: NASA/GSFC), available in electronic form from the NSSDC
Kniffen D.A., Bertsch D.L., Dingus B.L., et al., 1996, A&AS 120, 615C
Knödlseder J., Prantzos N., Bennett K., et al., 1996a, A&AS 120, 335C
Knödlseder J., von Ballmoos P., Diehl R., et al., 1996b, Proc. SPIE 2806, 386
Knödlseder J., Bennett K., Bloemen H., et al., 1999, A&A, in press
Knödlseder J., 1999, ApJ 510, 915
Oberlack U., Bennett K., Bloemen H., et al., 1996, A&AS 120, 311C
Oberlack U., 1997, Ph.D. Thesis, Technische Universität München
Phillipps S., Kearsey S., Osborne J.L., Haslam C.G.T., Stoffel H., 1981, A&A 98, 286
Prantzos N., 1991, In: Durouchoux Ph., Prantzos N. (eds.) Gamma-Ray Line Astrophysics. AIP, New York, 129
Prantzos N., 1993, ApJ 405, L55
Prantzos N., Diehl R., 1996 Phys. Rep. 267, 1
Reynolds R.J., 1984, ApJ 282, 191
Rothschild R., Boldt E., Holt S., et al., 1979, Sp. Sci. Instr. 4, 269
Schönfelder V., Aarts H., Bennett K., et al., 1993, ApJS 86, 657
Sodroski T.J., Odegard N., Dwek E., et al., 1995, ApJ 452, 262
Sodroski T.J., Odegard N., Arendt R.G., et al., 1997, ApJ 480, 173
Snowden S.L., Freyberg M.J., Plucinsky P.P., et al., 1993, ApJ 454, 643
Strong A.W., Cabeza-Orcel P., Bennett K., et al., 1992, In: Di Gesù V., et al. (eds.) Data Analysis in Astronomy - IV, Plenum Press, New York, 251
Thompson G.I., Nandy K., Jamar C., et al., 1978, A compilation of absolute stellar fluxes measured by the Sky Survey Telescope (S2/68) aboard the ESRO satellite TD-1. The Science Research Council, U.K.
Thompson D.J., Bertsch D.L., Dingus B.L., et al., 1995, ApJS 101, 259
Wainscoat R.J., Cohen M., Volk K., et al., 1992, ApJS 83, 111
Wright E.L., Mather J.C., Bennett C.L., et al., 1991, ApJ 381, 200